

Atomically engineered interfaces yield extraordinary electrostriction

Nini Pryds (✉ nipr@dtu.dk)

Technical University of Denmark <https://orcid.org/0000-0002-5718-7924>

Haiwu Zhang

DTU

Dae-Sung Park

Federal Institute of Technology-EPFL

Nicolas Gauquelin

University of Antwerp <https://orcid.org/0000-0002-5555-7055>

Simone Santucci

Technical University of Denmark

Dennis Christensen

Technical University of Denmark <https://orcid.org/0000-0003-0048-7595>

Daen Jannis

Electron Microscopy for Materials Science (EMAT), University of Antwerp

Dmitry Chezganov

Electron Microscopy for Materials Science (EMAT), University of Antwerp

Diana Rata

Institut für Physik, Martin-Luther-Universität Halle-Wittenberg

Ivano Castelli

Technical University of Denmark <https://orcid.org/0000-0001-5880-5045>

Johan Verbeeck

Electron Microscopy for Materials Research (EMAT), University of Antwerp

Igor Lubomirsky

Weizmann Institute

Paul Muralt

EPFL

Dragan Damjanovic

Ecole Polytechnique Fédérale de Lausanne <https://orcid.org/0000-0002-9596-7438>

Vincenzo Esposito

Technical University of Denmark

Keywords: electrostriction, atomically engineered interfaces, dielectric materials

Posted Date: June 24th, 2021

DOI: <https://doi.org/10.21203/rs.3.rs-615182/v1>

License:  This work is licensed under a Creative Commons Attribution 4.0 International License.

[Read Full License](#)

Version of Record: A version of this preprint was published at Nature on September 21st, 2022. See the published version at <https://doi.org/10.1038/s41586-022-05073-6>.

24 **Gd₂O₃-doped CeO₂ and Er₂O₃-stabilized δ -Bi₂O₃ with atomically controlled**
25 **interfaces on NdGaO₃ substrates. We find that the electrostriction coefficient**
26 **reaches $2.38 \times 10^{-14} \text{ m}^2/\text{V}^2$, exceeding the best-known relaxor ferroelectrics by three**
27 **orders of magnitude. Our atomic-scale calculations show that the extraordinary**
28 **electrostriction coefficient is driven by the coherent strain imparted by the**
29 **interfacial lattice mismatches. Thus, artificial heterostructures open a new avenue**
30 **to design and manipulate electrostrictive materials and devices for nano/micro**
31 **actuation and cutting-edge sensor applications.**

32 Materials developing strain in response to an electric field have attracted significant
33 attention over the previous several decades due to their wide applications, ranging from
34 non-resonant actuators, high-end transducers, artificial muscles, energy harvesting, and
35 various sensors.³⁻⁴ While piezoelectricity is limited to materials with a non-
36 centrosymmetric crystal structure, electrostriction is a general property of all dielectrics,
37 which produces a high displacement accuracy with the absence of strain-field hysteresis
38 and remnant polarization. However, the electrostriction coefficient (M_{xx}) is usually low,
39 attaining a value less than $10^{-19} \text{ m}^2/\text{V}^2$ for simple oxides such as MgO, TiO₂ and Y:ZrO₂.⁵
40 Owing to their very high electromechanical responses, the two archetypes of
41 electrostrictive materials are relaxor ferroelectrics and ferroelectric polymers.^{5, 6} The
42 former generates a significant electrostriction coefficient of $1.0 \times 10^{-17} \text{ m}^2/\text{V}^2$ with
43 mechanical stress of 150 MPa or less.^{7, 8} In contrast, flexible polymers exhibit high

44 electrostrictive coefficients up to $1.8 \times 10^{-18} \text{ m}^2/\text{V}^2$ while the stress delivered is about two
45 orders of magnitude lower (2 MPa on average).⁹

46

47 A new family of high-performance electrostriction materials was recently discovered in
48 Gd_2O_3 -doped CeO_2 (CGO), exhibiting anomalously large electrostriction with the
49 maximum stress exceeding 500 MPa.^{10,11} The investigated CGO-based films have
50 typically large thicknesses ($t > 300 \text{ nm}$), where the in-plane biaxial strain is fully relaxed,
51 and the M_{xx} is improved by less than one order of magnitude compared to the bulk
52 counterparts, i.e., 10^{-17} vs $10^{-18} \text{ m}^2\text{V}^{-2}$.^{10, 13-15}

53

54 Over the past decade, increased interest has been placed in the growth of ultrathin
55 complex oxide heterostructures. These films exhibit superior properties, such as fast ionic
56 conduction,¹⁶ metal-to-insulator transition,¹⁷ and ferroelectricity in otherwise paraelectric
57 materials.¹⁸ Such emergent properties are associated with the complex yet tailorable
58 interfacial morphology that gives rise to ionic/electronic redistribution, symmetry
59 breaking and strain gradients.^{1,2} For ferroelectric thin films, the evolution of electric
60 polarization with reduced film thickness has been one of the crucial topics in the field,
61 with interfaces and surfaces playing a pivotal role.¹⁹⁻²³ However, to date, the effects of
62 interfaces and synthesis of ultrathin films ($\ll 100 \text{ nm}$) on the electrostriction property
63 has not been explored.

64

65 Here, we demonstrate a new concept of engineering electrostriction through artificial
66 interfaces. We selected Gd₂O₃-doped CeO₂ (CGO) and Er₂O₃-stabilized δ -Bi₂O₃ (ESB)
67 as the two model material systems. We designed the multilayers to achieve two purposes:
68 1) to establish an interfacial configuration where the lattice mismatch can be used as a
69 tuning knob and 2) to confine the electrostrictive layers by selecting a set of two materials
70 that develop desired lattice distortions under an electric field. With this strategy, we
71 achieved an electrostrictive enhancement of three orders of magnitude when compared to
72 thick CGO films, reaching the highest value ($M_{xx} \sim 10^{-14} \text{ m}^2/\text{V}^2$) measured so far in any
73 electrostrictive material. This artificial electrostrictive heterostructure paves a new way
74 for achieving extraordinary electrostriction, yielding new opportunities for nano/micro
75 electrostrictive devices.

76

77 Ultrathin films were deposited by pulsed laser deposition (PLD). The heterostructures
78 consist of alternating layers of gadolinium-doped ceria (Ce_{0.8}Gd_{0.2}O_{1.9}, CGO) and
79 erbium-stabilized bismuth oxide (Er_{0.4}Bi_{1.6}O₃, ESB) deposited on pseudocubic (pc) [010]-
80 oriented NdGaO₃ substrates (NGO). The heterostructures are defined as
81 NGO/CGO/[ESB/CGO]_N, where $N = \{1, 3, 7, 10, 15\}$ is the number of [ESB/CGO]
82 bilayers as schematically illustrated in Fig. 1a. The total thickness of the thin films was
83 fixed at about 17 nm with a ratio of 1:1 of CGO and ESB. We define a modulation length

84 (λ) as the thickness of the [ESB/CGO] bilayers with values of 8.5, 2.8, 1.2, 0.9 and 0.6
85 nm, corresponding to $N = 1, 3, 7, 10$ and 15 , respectively. High-angle annular dark-field
86 scanning transmission electron microscopy (HAADF-STEM) Z-contrast images of
87 NGO/CGO/[ESB/CGO]₇ reveal the epitaxial relationship between the constituent layers,
88 with ESB exhibiting a brighter ADF image contrast than CGO (Fig. 1b). Atomically
89 resolved EDX profiles of Ce, Er and O show the compositional variation from which
90 well-defined interfaces can be identified. Up to a value of $N = 7$ and $\lambda = 1.2$ nm, we
91 observe no sign of dopant segregation or formation of extended defects (e.g. dislocations
92 or line defects). However, a further increase of N to 10 ($\lambda=0.9$ nm) results in significant
93 chemical intermixing, indicating the collapse of the heterostructure (Extended Data Fig.
94 1).

95

96 The electrostrictive response of the 17 nm thick multilayer deposited on an NGO
97 cantilever is proportional to the square of the electric field strength (Extended Data Fig.
98 2). The maximum stress generated in this configuration was 9.7 GPa. Fig. 1c shows the
99 electrostriction coefficient (M_{xx}) of the multilayers as a function of the modulation length
100 measured at 1 Hz. For ease of comparison, the electrostriction coefficients (M_{xx}) of a
101 single layer of CGO thin film ($t = 17$ nm) deposited on NGO are also shown, as well as a
102 range of thick CGO films ($t \geq 400$ nm) deposited on different substrates taken from the
103 literature.^{10,14,15} Comparisons with Bi₂O₃-based films are not included as their

104 electrostrictive properties have not been investigated due to their structural and chemical
105 instabilities.^{11, 24, 25} As seen in Fig. 1c, the measured electrostriction coefficients exhibit a
106 "volcano-like" shape as a function of the modulation length, reaching a maximum at $N =$
107 7 ($\lambda = 1.2$ nm). The electrostriction coefficients generally follow a linear increase as the
108 modulation length decreases down to 1.2 nm. Different materials' values reported in the
109 literature follow the same trend, regardless of the deposition methods, process parameters,
110 microstructure of the films and type of substrate/electrode.^{10, 14, 15, 26} Remarkably, for the
111 first time, we show that the maximum M_{xx} of the heterostructure (2.38×10^{-14} m²/V²)
112 surpasses that of the thick CGO films by more than three orders of magnitude.^{10, 14, 15, 26}
113 However, as λ decreases below $\lambda = 1.2$ nm ($N > 7$) the electrostriction coefficient
114 decreases significantly. This effect relates to intermixing at the interfaces (Extended Data
115 Fig. 1) and the corresponding decrease in the electrostrictive performance.

116

117 We have systematically investigated the performance of the heterostructures with
118 different stacking sequences where the deposition on NGO was started with either CGO
119 or ESB. When ESB was deposited directly on NGO (NGO/ESB/[CGO/ESB]₇), the
120 heterostructure is unstable and shows a reduced electrostriction coefficient of 3.0×10^{-16}
121 m²/V² (Extended Data Fig. 3). In contrast, when CGO was deposited on NGO
122 (NGO/CGO/[ESB/CGO]₇), the heterostructure was stable and exhibited a significantly
123 enhanced electrostriction, highlighting the importance of the stacking sequence. We thus

124 used NGO/CGO/[ESB/CGO]_N as the main configuration in our experiments, ensuring
125 that the heterostructure is capped with CGO to avoid degradation of the ESB. Fig. 1d
126 shows the electrostriction coefficient, M_{xx} , for heterostructures with $N = 1$ ($A = 12.0$ nm),
127 $N = 7$ ($A = 1.21$ nm) and $N = 15$ ($A = 0.57$ nm) as a function of the frequency. Our results
128 outperformed any known electrostrictive materials, including bulk CGO,²⁶ Y/Nb:Bi₂O₃,¹¹
129 La₂Mo₂O₉,²⁷ Y:ZrO₂ (YSZ)¹¹ as well as the commercial relaxor ferroelectrics, such as
130 Pb(Mg_{1/3}Nb_{2/3})O₃-PbTiO₃ (PMN-PT),⁶ P(VDF-TrFE) copolymers⁹ and the recently
131 discovered ultrahigh electrostriction in lead halide perovskites.²⁸ Similar to bulk CGO,
132 the electrostriction coefficient of the heterostructures decreases when the frequency is
133 increased ($1 < f < 200$ Hz). The measured M_{xx} decreases from 2.38×10^{-14} at 1 Hz to
134 3.76×10^{-15} m²/V² at 200 Hz for $N = 7$. The enhancement in the electrostrictive response
135 may lead to novel applications, as it permits a significant decrease in the operating
136 electrical field, which improves the long-term stability of the devices.

137

138 One potential drawback associated with multilayers is the possible delamination at the
139 interfaces after cyclic electrical loading, leading to the failure of the electrostrictive
140 devices. Therefore, we have evaluated the fatigue behaviour of NGO/CGO/[ESB/CGO]₇
141 as a function of time at a constant electric field of 17.4 kV cm⁻¹. The field-induced stress
142 shows no sign of degradation and remains stable after 1000 cycles at 1 Hz. Subsequent

143 measurements further confirm the mechanical stability at 50 and 200 Hz for another 1000
144 cycles, respectively (Extended Data Fig. 4).

145

146 We have performed structural analysis to rationalize the exceptionally large
147 electrostriction coefficients. Fig. 2a shows the reciprocal space mappings (RSMs) around
148 the asymmetric $(221)_{\text{pc}}$ reflection of NGO for different heterostructures with different N .
149 The out-of-plane position and shape of the (420) reflections of the heterostructures change
150 with increasing N . The overall structural coherency is essentially maintained, indicating
151 that the in-plane lattice parameters of the heterostructure are coherent with respect to the
152 substrate, which is in line with the STEM results. The sub-peaks along (110) observed
153 for $N = 1$, and 3 and along the (004) are attributed to the lattice relaxations within the
154 CGO and ESB layer. X-ray diffraction (2θ - ω scan) analysis reveals that the
155 heterostructures are phase-pure films oriented along the (110) crystallographic direction
156 (Fig. 2b). A minor signal of (111) orientation is observed for the $N = 3, 7$ and 15 (results
157 are not shown here). The Laue diffraction oscillations around the superlattice peaks
158 originate from the coherency between individual sublayers and indicate smooth interfaces
159 between the ESB and CGO layers (Fig. 2b), aligning well with the STEM results (Fig.
160 1b). To accommodate the significant mismatch and allow cube-on-cube growth, the
161 fluorite oxide (CGO) grows epitaxially on the perovskite oxide (NGO) by allowing a
162 rotation of 45° . This arrangement results in an epitaxial relationship of

163 $\langle 110 \rangle_{\text{CGO}} // \langle 010 \rangle_{\text{pc NGO}}$ (see also Extended Data Fig. 1a) and a significant decrease in the
164 mismatch to $\sim 1\%$ (See Fig. 2c).

165

166 For the heterostructure (NGO/CGO/[ESB/CGO]_N), the lattice mismatch to the substrate
167 is entirely compensated by elastic strain, generating an average in-plane strain of 1% (see
168 Fig. 2d). On the other hand, the magnitude of the average out-of-plane strain decreases
169 when increasing N from 1 to 7. The minimum strain value is observed at $1/\Lambda = 0.8 \text{ nm}^{-1}$
170 with the abnormal strain change for $1/\Lambda > 0.8 \text{ nm}^{-1}$ attributed to the chemical intermixing
171 at the interfaces, as shown in the EELS and EDX maps in Extended Data Fig. 1b and c.
172 The minimum in the out-of-plane lattice parameters at $1/\Lambda = 0.8 \text{ nm}^{-1}$ correlates well with
173 the measured modulation length-dependent electrostriction coefficient (Fig. 1c).

174

175 We next performed atomic-scale simulations on CGO/ESB heterostructures to understand
176 the structural evolution as a function of modulation length (Fig. 2). The model structures
177 are optimized with the in-plane lattice parameters fixed to the NGO substrate, while the
178 out-of-plane lattice parameter is allowed to relax. The calculations were carried out for
179 alternating layers of CGO and ESB with different modulation lengths, corresponding to
180 96, 48, 32, 24, 16, 12, 8, 6 and 4 cationic planes, respectively (see Method section). Fig.
181 3a is a schematic illustration of the modulation length, and the definition of the cationic
182 interplanar distance (d_C) projected onto the out-of-plane direction. The amplitude of

183 CGO/ESB interfacial coupling is captured by the variation of d_C as a function of
184 modulation length (Fig. 3b). For example, for $\Lambda = 18.56$ nm (96 cationic planes), the
185 lattice relaxation yields two distinct plateaus at 1.92 and 1.96 Å, close to the individual
186 interplanar distances of bulk CGO and ESB, respectively. This range of values agrees
187 well with the lattice relaxation observed for $N = 1$ and $N = 3$ in the RSMs shown in Fig.
188 2a.

189

190 With the decrease of Λ , the interfacial coupling becomes progressively evident. By further
191 reducing Λ towards 1.55 nm and beyond (approaching the modulation length of 1.2 nm
192 for NGO/CGO[ESB/CGO]₇), the interplanar distances become gradually frustrated. At Λ
193 = 0.78 Å, the discrimination between the interfaces and individual regions becomes
194 difficult. The structural evolution is also associated with a peak maximum ($1/\Lambda = 0.8$ nm⁻¹
195 ¹) in the out-of-plane lattice parameter in which above the modulation length decreases
196 as shown in Fig. 3c. Remarkably, the results obtained from the atomic-scale simulations
197 agrees well with the results obtained from the X-ray diffractions and the electrostrictive
198 measurements (Fig. 1c). The above results reveal a clear correlation between the
199 electromechanical properties and the epitaxial strain.

200 To further understand the relationship between the electromechanical properties, the
201 modulation length and strain, we perform molecular dynamics (MD) simulations on
202 heterostructures with different modulation lengths and biaxial strain (ϵ^*). Fig. 4a shows

203 the calculated Helmholtz free energy (F) as a function of the biaxial strain for the
204 heterostructure with $\lambda = 1.55$ nm (12 cationic layers), which is close to the maximum
205 electrostrictive effect (Fig. 1c). The system has the lowest total energy (F) in the absence
206 of strain and increasing free energy when compressive or tensile strains are applied. The
207 free energy increases at a specific strain value and exhibits a maximum function of $1/\lambda$
208 (Fig. 4b). This effect is attributed to the enhanced interlayer interactions, as CGO and
209 ESB couple at the interfaces.

210

211 Applying an electrical field of $E = 20$ kV/cm along the $+x$ direction causes an energy
212 difference $\Delta F = F_{E = 20 \text{ kV/cm}} - F_{E = 0}$, which is shown in Fig. 4c as a function of λ and
213 different ϵ^* . Interestingly, ΔF has a parabolic behaviour as a function of $1/\lambda$, indicating a
214 linear relationship between ΔF and $(1/\lambda)^2$. Assuming that the in-plane and out-of-plane
215 lattice parameters are allowed to relax, the energy change, ΔF , will be dominated by the
216 elastic energy due to the strain developed (Δu). Thus, ΔF relates to Δu following Hooke's
217 law: $\Delta F \propto (\Delta u)^2$. Since the electrostriction coefficient M_{xx} is directly proportional to Δu ,
218 one could derive the following relationship $(M_{xx})^2 \propto (\Delta u)^2 \propto \Delta F \propto (1/\lambda)^2$, which indicates
219 that $M_{xx} \propto 1/\lambda$. This relation is in a reasonable agreement with the relationship observed
220 experimentally, although the experimental values of M_{xx} increases slightly faster, *i.e.*, M_{xx}
221 $\propto (1/\lambda)^{1.3}$ (see Fig. 1c). Similarly, a tensile strain would drive the system away from its
222 ground state to a higher energy state (see Fig. 4a). Therefore, a larger field-induced lattice

223 change could be generated, allowing the heterostructure to contract when E is applied
224 parallel to the (100) direction (Extended Data Fig. 5).

225

226 The electrostrictive effect is further confirmed by inspecting the response of local
227 distortions to the electric field. To describe the collective contribution of such local
228 distortions, we have extracted the electric dipoles induced by defects and the
229 displacements of cations and anions (Extended Data Fig. 6 and the Method part). Fig. 4d
230 presents the dipole distribution within the heterostructure ($\lambda = 4.65$ nm) for $\varepsilon^* = +0.05$ at
231 300 K in the absence of an electric field. It is clear from this figure that various local
232 configurations exist, and there is no apparent ordered arrangement of local distortions. By
233 applying a large electrical field ($E = 30$ kV/cm) along the $+x$ direction, the distribution of
234 electric dipoles becomes skewed in $+x$ direction (Fig. 4e). This effect corresponds to a
235 more ordered structure with dipoles aligning along the external electric field.
236 Simultaneously, the density and magnitude of the dipoles increase substantially due to
237 the off-centre displacements of cation and anions. Fig. 4f summarises the normalized
238 probability distribution function, $P(\mu_x)$, against the normalized magnitude of the electric
239 dipole moments along the x -axis (μ_x) for heterostructures with different λ under the same
240 tensile strain ($\varepsilon^* = +0.05$). With the absence of an electric field, the dipoles exhibit a broad
241 and symmetric distribution. This configuration gives rise to a zero macroscopic
242 polarisation (Fig. 4f solid line). However, applying an electric field along the $+x$ direction

243 induces an asymmetric probability function with the peak in $P(\mu_x)$ shifted to higher
244 values, demonstrating the alignment of the dipoles along the direction of the electrical
245 field. With the decrease of λ , the dipoles become less resistive to changes in the electrical
246 field. Therefore, the alignment along the $+x$ direction is increasingly favoured. Such facile
247 structural variations are responsible for increasing the change in energy and
248 electrostrictive performance when decreasing the modulation length.

249

250 By engineering the electrostrictive materials with specifically designed interfaces, we
251 demonstrated a significantly enhanced electrostriction coefficient surpassing any other
252 known electrostrictive materials. These results produce a framework for engineering
253 electrostrictive properties in heterostructures. It also offers new opportunities for
254 designing and manipulating the performance of electrostrictive materials, e.g., for optical
255 communications, which is at the heart of commercial technologies such as digital light-
256 processing and optical switches and sensing and imaging devices with long-term stability.
257 Unlike the toxic lead-based ferroelectrics such as PMN-PT and MAPbI_3 , the current
258 electrostrictive materials are environmentally friendly, making them suitable for a wide
259 range of biomedical actuation and micro-sensors applications.

260

261 **Online content**

262 Any methods, additional references, Nature Research reporting summaries, source data,
263 extended data, supplementary information, acknowledgements, peer review information;
264 details of author contributions and competing interests; and statements of data and code
265 availability are available at <http://npg.nature.com>

266

267 1. Ramesh, R. & Schlom, D. G. Creating emergent phenomena in oxide superlattices. *Nat. Rev. Mater.* **4**,
268 257-268 (2019).

269 2. Yang, M. M. Luo, Z., D. Zhao., J. Alexe, M., Piezoelectric and pyroelectric effects induced by interface
270 polar symmetry. *Nature*. **584**, 377-381 (2020).

271 3. Li, F., Jin, L., Xu, Z. & Zhang, S. Electrostrictive effect in ferroelectrics: An alternative approach to
272 improve piezoelectricity. *Appl. Phys. Rev.* **1**, 011103 (2014).

273 4. Kremer, F. et al. Giant lateral electrostriction in ferroelectric liquid-crystalline elastomers. *Nature*. **410**,
274 447-450 (2001).

275 5. Yimmirun, R., Moses, P. J., Newnham, R. E. & Meyer, R. J. Electrostrictive strain in low-permittivity
276 dielectrics. *J. Electroceramics*. **8**, 87-98 (2002).

277 6. Li, F., Jin, L., Xu, Z., Wang, D. & Zhang, S. Electrostrictive effect in $\text{Pb}(\text{Mg}_{1/3}\text{Nb}_{2/3})\text{O}_3\text{-xPbTiO}_3$ crystals.
278 *Appl. Phys. Lett.* **102**, 152910 (2013).

279 7. Zednik, R. J., Varatharajan, A., Oliver, M., Valanoor, N. & McIntyre, P. C. Mobile ferroelastic domain
280 walls in nanocrystalline PZT films: The direct piezoelectric effect. *Adv. Funct. Mater.* **21**, 3104-3110
281 (2011).

- 282 8. Li, F. et al. Ultrahigh piezoelectricity in ferroelectric ceramics by design. *Nat. Mater.* **17**, 349-354 (2018).
- 283 9. Zhang, Q. M., Bharti, V. & Zhao, X. Giant electrostriction and relaxor ferroelectric behavior in electron-
284 irradiated poly(vinylidene fluoride-trifluoroethylene) copolymer. *Science*. **280**, 2101-2104 (1998).
- 285 10. Korobko, R. et al. Giant electrostriction in Gd-doped ceria. *Adv. Mater.* **24**, 5857-5861 (2012).
- 286 11. Yavo, N. et al. Large Nonclassical Electrostriction in (Y, Nb)-Stabilized δ -Bi₂O₃. *Adv. Funct. Mater.*
287 **26**, 1138-1142 (2016).
- 288 12. Cancellieri, C. et al. Electrostriction at the LaAlO₃/SrTiO₃ interface. *Phys. Rev. Lett.* **107**, 1-4 (2011).
- 289 13. Korobko, R. et al. In-situ extended X-ray absorption fine structure study of electrostriction in Gd doped
290 ceria. *Appl. Phys. Lett.* **106**, 042904 (2015).
- 291 14. Hadad, M., Ashraf, H., Mohanty, G., Sandu, C. & Murali, P. Key-features in processing and
292 microstructure for achieving giant electrostriction in gadolinium doped ceria thin films. *Acta Mater.* **118**,
293 1-7 (2016).
- 294 15. Santucci, S., Zhang, H., Sanna, S., Pryds, N. & Esposito, V. Enhanced electromechanical coupling of
295 TiN/Ce_{0.8}Gd_{0.2}O_{1.9} thin film electrostrictor. *APL Mater.* **7**, 0-5 (2019).
- 296 16. Sata, N., Eberman, K., Eberl, K. & Maier, J. Mesoscopic fast ion conduction in nanometre-scale planar
297 heterostructures. *Nature*. **408**, 946-949 (2000).
- 298 17. Domínguez, C. et al. Length scales of interfacial coupling between metal and insulator phases in oxides.
299 *Nat. Mater.* **19**, 1182-1187 (2020).
- 300 18. Haeni, J. H. et al. Room-temperature ferroelectricity in strained SrTiO₃. *Nature*. **430**, 758-761 (2004).

- 301 19. Junquera, J. & Ghosez, P. Critical thickness for ferroelectricity in perovskite ultrathin films. *Nature*.
302 **422**, 506-509 (2003).
- 303 20. Fong, D. D. et al. Ferroelectricity in ultrathin perovskite films. *Science*. **304**, 1650-1653 (2004).
- 304 21. B. K. Mani, C.-M. Chang, S. Lisenkov, and I. P. Critical Thickness for Antiferroelectricity in PbZrO₃.
305 *Phys. Rev. Lett.* **097601**, 1-5 (2015).
- 306 22. Zhang, W. & Ouyang, J. Interface engineering of ferroelectric thin-film heterostructures.
307 Nanostructures in Ferroelectric Films for Energy Applications: Domains, Grains, Interfaces and
308 Engineering Methods (Elsevier Inc., 2019). doi:10.1016/B978-0-12-813856-4.00006-5
- 309 23. Ji, D. et al. Freestanding crystalline oxide perovskites down to the monolayer limit. *Nature*. **570**, 87-90
310 (2019).
- 311 24. Sanna, S. et al. Enhancement of the chemical stability in confined δ -Bi₂O₃. *Nat. Mater.* **14**, 500-504
312 (2015).
- 313 25. Sanna, S. et al. Structural instability and electrical properties in epitaxial Er₂O₃-stabilized Bi₂O₃ thin
314 films. *Solid State Ionics*. **266**, 13-18 (2014).
- 315 26. Varenik, M. et al. Dopant concentration controls quasi-static electrostrictive strain response of ceria
316 ceramics. *ACS Appl. Mater. Interfaces*. **12**, 39381-39387 (2020).
- 317 27. Li, Q. et al. Giant thermally-enhanced electrostriction and polar surface phase in La₂Mo₂O₉ oxygen ion
318 conductors. *Phys. Rev. Mater.* **2**, 1-7 (2018).
- 319 28. Chen, B. et al. Large electrostrictive response in lead halide perovskites. *Nat. Mater.* **17**, 1020-1026
320 (2018).

321 **Acknowledgements**

322 This research was supported by the BioWings project funded by the European Union's
323 Horizon 2020, Future and Emerging Technologies (FET) programme (Grant No. 801267)
324 and Danish Council for Independent Research Technology and Production Sciences for
325 the DFF- Research Project 2 (Grant No. 48293). N.P. acknowledges the funding from
326 Villum Fonden for the NEED project (00027993) and Danish Council for Independent
327 Research Technology and Production Sciences for the DFF- Research Project 3 (Grant
328 No. 00069B). V.E. acknowledges the funding from Villum Fonden for the IRIDE project
329 (00022862). N.G. and J.V. acknowledge funding from the GOA project "Solarpaint" of
330 the University of Antwerp. The microscope used in this work was partly funded by the
331 Hercules Fund from the Flemish Government. D.J. acknowledges funding from FWO
332 Project G093417N from the Flemish fund for scientific research. D.C. acknowledge
333 TOP/BOF funding of the University of Antwerp. This project has received funding from
334 the European Union's Horizon 2020 Research Infrastructure - Integrating Activities for
335 Advanced Communities under grant agreement No 823717-ESTEEM3. The authors
336 would like to thanks Thierry Dèsirè Pomar for the English proofreading.

337

338 **Author Contributions**

339

340 H. Z., N. P. and V.E. conceived the idea and designed the project. H.Z. and S.S. prepared
341 the samples and characterized the electromechanical properties. N.G. performed the
342 STEM measurements and analyzed the STEM-EELS results. D.J. helped with the
343 processing of the HAADF-STEM data analysis, and D.C. did the statistical analysis of

344 the EDX results under the supervision of N.G. and J.V. D.P. and R.D. performed the XRD
345 and RSMs characterization. H. Z. and I. E.C. performed the atomic-scale simulations. D.
346 V.C. performed the finite element simulations. H.Z. and N.P. wrote the manuscript with
347 input from all the authors. All authors have read and agreed to the published version of
348 the manuscript.

349 **Competing interests** The authors declare no competing financial interests.

350

351 **Additional information**

352

353 **Supplementary information** is available for this paper at www.nature.com.

354 **Correspondence and requests for materials** should be addressed to H. Z, V.E and N. P.

355 **Reprints and permissions** information is available online at <http://npg.nature.com/reprintsandpermissions>.

356

357 **Methods**

358 **Thin-film fabrication.** The heterostructures are fabricated by alternating CGO and ESB
359 layers using pulsed laser deposition (PLD) with a multi-target carousel. The target-
360 substrate distance was 50 mm. The 248 nm KrF excimer laser was operated at 2 Hz with
361 a laser fluency of 1.8 J/cm². The deposition rate is ~0.05 nm per pulse. The total number
362 of laser shots on the targets is 3560 (1780 for CGO and 1780 for ESB), giving rise to a
363 total thickness of ~17 nm. The ratio of CGO and ESB is fixed at 1:1, whereas the thickness
364 of each layer varies with modulation length. The deposition was performed at 600 °C at
365 an oxygen partial pressure of 10⁻³ mbar. The heating/cooling rate is 10 °C/min. The Au
366 top electrodes are sputtered with a Bal-Tec SCD 005 Sputter Coater at room temperature.

367 **STEM, EDX and EELS measurement.** The cross-section TEM lamellas were prepared
368 via focused ion beam (FIB) using a FEI HELIOS 650 dual-beam Focused Ion Beam device.
369 During the preparation process, carbon and platinum protective layers were deposited on
370 top of the film. The aberration-corrected high angular annual dark-field scanning
371 transmission electron microscopy (HAADF-STEM) and energy-dispersive X-ray
372 spectroscopy (EDX) were performed on a probe aberration-corrected 'cubed' FEI TITAN
373 80-300 electron microscope operated at 300 kV equipped with SUPER-X EDX detector
374 system. Line profiles of elemental distribution along the TEM lamellas were averaged
375 over several unit cells laterally for better statistics. Electron energy loss spectroscopy
376 (EELS) data were acquired on a double aberration-corrected 'cubed' FEI TITAN 80-300
377 electron microscope operated at 120 kV in monochromated mode, providing an energy
378 resolution of 150 meV.

379 **XRD and RSMs analysis.** The crystal structure and the strain states were characterized
380 by a high-resolution Bruker D8 discover diffractometer with monochromatic Cu $K_{\alpha 1}$
381 radiation ($\lambda=1.5406 \text{ \AA}$). The reciprocal space mappings were performed around the (221)
382 asymmetric reflection of the NGO substrate.

383 **Electrostriction measurements.** The electrostriction properties of the
384 NGO/CGO/[ESB/CGO]_N heterostructures were measured with a planar electrode
385 configuration, with the two electrodes placed on the top of the thin films in parallel (Fig.
386 S4). This configuration avoids using the bottom electrode, thus facilitating the substrate's
387 choice with desired lattice mismatch (and therefore biaxial strain).²⁹ The sinusoidal
388 electric field was generated by AIM-TTI TGP 3100 function generator, amplified by a
389 Trek 2220 amplifier. During the measurement, one end of the cantilever was clamped.

390 The oscillation of the free end was measured using a single-beam laser interferometer
 391 SIOS NA analyzer at the 2nd-harmonic of the electrical field. An Ametek 7230 DSP Lock-
 392 in Amplifier was used to improve the signal-noise ratio (down to 0.2 nm). Such a
 393 measuring configuration yields the longitudinal electrostriction coefficient (M_{13}) of the
 394 heterostructures (Extended Data Fig. 5a). However, M_{xx} is used for ease of comparison
 395 with results taken from the literature.

396 **Atomic-scale simulations.** Atomic-scale simulations were performed based on the well-
 397 established classical simulation approach to model the various possible distributions of
 398 the point defects within the heterostructures. The interatomic interactions are described
 399 by:

$$400 \quad V_{ij} = \frac{Z_i Z_j}{4\pi\epsilon_0 r_{ij}} + A_{ij} \exp\left(-\frac{r_{ij}}{\rho_{ij}}\right) - \frac{C_{ij}}{r_{ij}^6}$$

401 where the first term describes the long-range Columb interactions, and the following two
 402 terms correspond to the short-range electron cloud overlap and dispersions, respectively.
 403 The parameters, r_{ij} , $Z_{i(j)}$ and ϵ_0 are the distance between ions i and j , the ion's valences,
 404 the permittivity of free space, respectively. A_{ij} , ρ_{ij} and C_{ij} are the empirical Buckingham
 405 parameters (listed in Extended Data Fig. 7a).

406 The molecular dynamics (MD) were performed with the following steps: 1) Construct
 407 the (100)×(0 $\bar{1}$ 1)×(011)-orientated heterostructures with various modulation length; 2)
 408 Introduce the dopants and oxygen vacancies at random; 3) Apply biaxial strains by
 409 adjusting the in-plane lattice parameters to specific values; 4) Equilibrate the structures

410 at 2400 K for 600 ps, followed by another equilibration at 300 K for 300 ps; 5) Turn on
411 the electrical field along the (100)-crystallographic direction at 300 K and extract the
412 optimized structures and free energies after 100 ps. During the simulations, the in-plane
413 lattices parameters are fixed, whilst the out-of-plane lattice parameters are free to relax.
414 The pressure was kept constant (1.01 mbar), and the temperature was monitored by a
415 Nosé-Hoover thermostat (*NPT* ensemble),^{30,31} as implemented in the LAMMPS package.³²
416 Large supercells of $10 \times 8\sqrt{2} \times 24\sqrt{2}$ (41472 atoms) and $16 \times 12\sqrt{2} \times 12\sqrt{2}$ (49768
417 atoms) were used to model the interfacial coupling (Fig. 3) and the modulation length and
418 strain (Fig. 4), respectively.

419 The electronic dipoles were calculated to describe the local distortions and their
420 response to the electric field. The analysis was realized by dividing the period simulation
421 box into $N \times N \times N$ cubes, where the side length of each cube is $L_{\text{cube}} = L_{\text{box}}/N$. For
422 visualizing and statisting of the dipoles, the period simulation box was divided into 4×4
423 $\times 4$ and $8 \times 8 \times 8$ cubes, respectively. By summing the point charges within the i th cube,
424 the net positive charge (q_i^+) and negative charge (q_i^-) and the distance (\vec{r}_i) between q_i^+
425 and q_i^- were determined. The dipole moment was then calculated by $\vec{\mu}_i = q_i \vec{r}_i$, the
426 direction of which is parallel to the vector pointing from q_i^- to q_i^+ in the i th cube.
427 Extended Data Fig. 8 schematically illustrated the appearance of electronic dipoles
428 induced by the defects within CeO₂ and δ -Bi₂O₃.

429

430 **Data Availability**

431 The data that support the findings of this study are available from the corresponding
432 authors upon reasonable request.

433

434 29. Nigon, R., Raeder, T. M. & Murali, P. Characterization methodology for lead zirconate titanate thin
435 films with interdigitated electrode structures. *J. Appl. Phys.* **121**, 204101 (2017).

436 30. Nosé, S. A unified formulation of the constant temperature molecular dynamics methods. *J. Chem.*
437 *Phys.* **81**, 511-519 (1984).

438 31. William G. Hoover. Canonical dynamics: Equilibrium phase-space distributions William. *Phys. Rev. A.*
439 **31**, 1695-1697 (1985).

440 32. Plimpton, S. Fast Parallel Algorithms for Short-Range Molecular Dynamics. *J. Comput. Phys.* **117**, 1-
441 19 (1995).

442

443

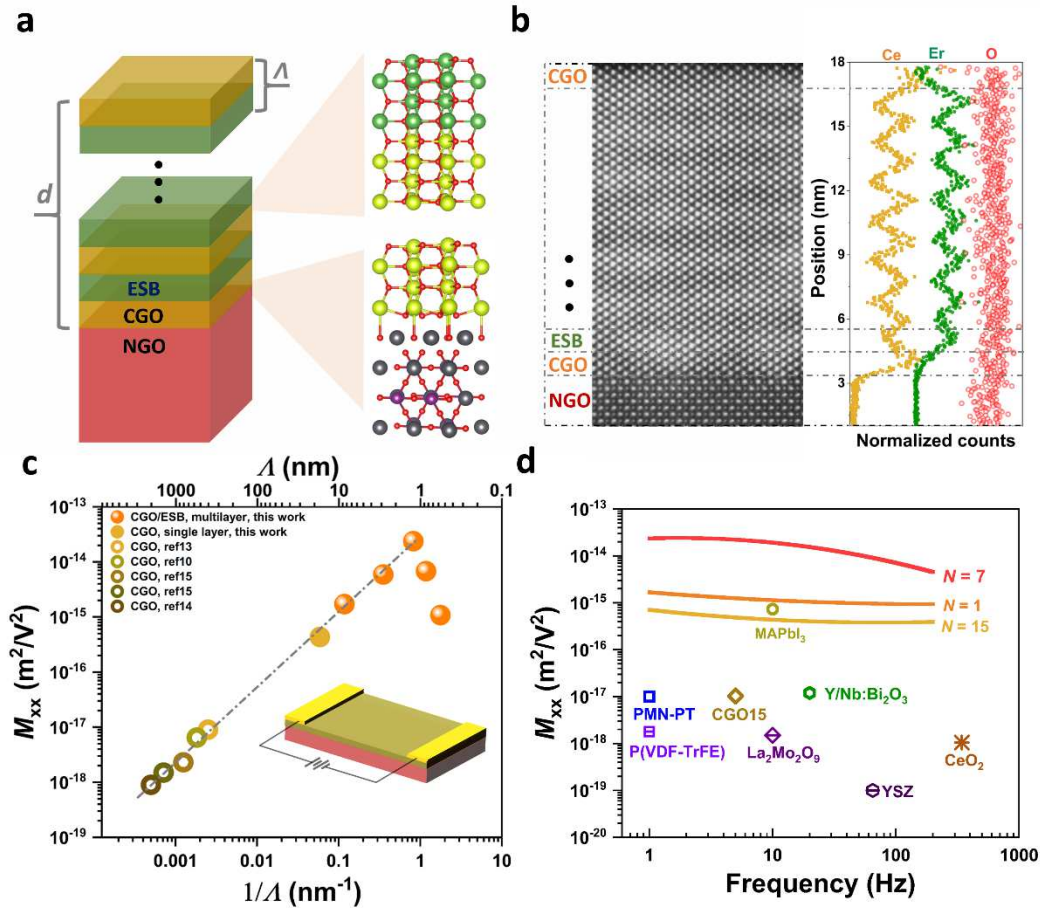
444

445

446 **Figure legends:**

447

448 **Figure 1**



449

450 **Fig. 1| Multilayer structure and electrostrictive property of NGO/CGO/[ESB/CGO]_N.** a, Schematic illustration of

451 the multilayer architecture. b, STEM-HAADF image and EDX compositional variations for $N = 7$. c, Electrostriction

452 coefficient (M_{xx}) as a function of modulation length (λ) measured at 1 Hz. For single layered films, λ is the total

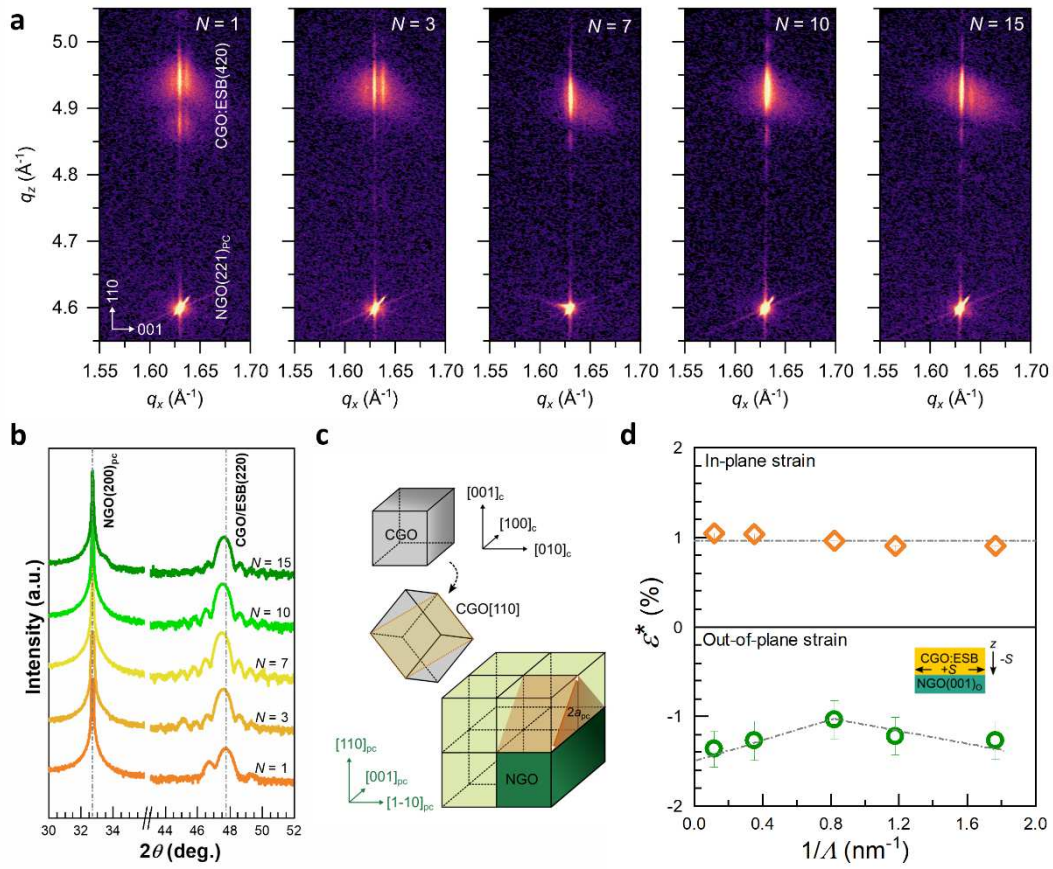
453 thickness. The inset schematically illustrate the top-top electrode configuration. d, Electrostriction coefficient (M_{xx}) as

454 a function of frequency for heterostructures with $N = 1, 7$ and 15. Electrostriction properties of various electrostrictive

455 materials are shown for comparison: CeO_2 ,²⁶ CGO15,²⁶ Y/Nb: Bi_2O_3 ,¹¹ YSZ,¹¹ $\text{La}_2\text{Mo}_2\text{O}_9$,²⁷ PMN-PT,⁶ P(VDF-TrFE),⁹

456 and MAPbI₃.²⁸

474 **Figure 2**



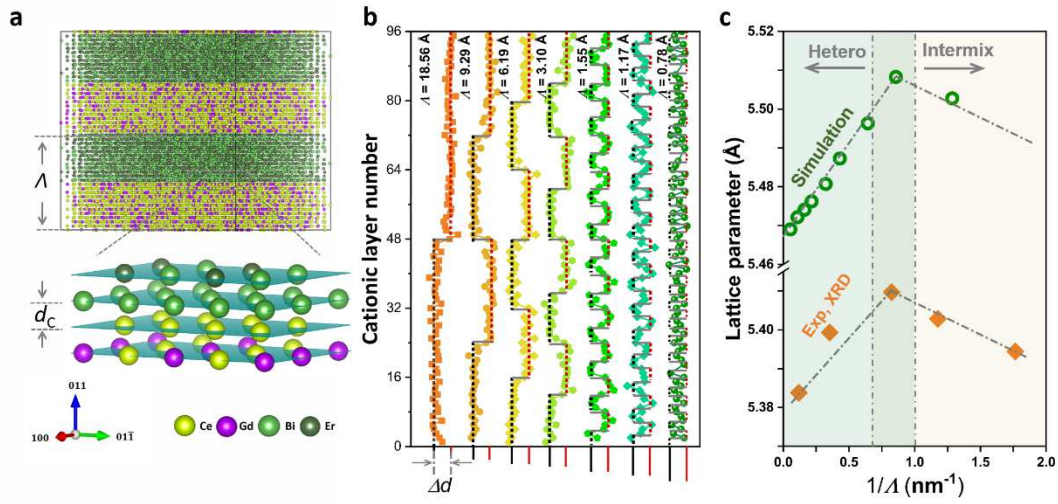
475

476 **Fig. 2| Structure analysis for NGO/CGO/[ESB/CGO]_N.** **a**, Reciprocal space mappings (RSMs) of the
 477 NGO/CGO/[ESB/CGO]_N heterostructures around the asymmetric (221)_{pc} reflection of the NGO substrate. **b**, X-ray
 478 diffraction pattern (2θ - ω scans) of the films. **c**, Schematic illustration of the epitaxial relationship of the heterostructure
 479 with respect to the NGO substrate. **d**, the evolution of the in-plane and out-of-plane strains. The in-plane and out-of-
 480 plane strains are calculated based on the RSMs and 2θ - ω scans, respectively. The error bars in **d** represent the fitting
 481 error of the lattice constants.

482

483

484 **Figure 3**



485

486 **Fig. 3 | Mechanism of interlayer interaction.** **a**, Schematic illustration of the modulation length (λ) and the cationic

487 interplanar distance (d_c) for heterostructures. The oxygen ions are omitted for clarity. **b**, The variation of d_c as a

488 function of λ projected onto the out-of-plane direction. The dark and red dot lines represent the individual interplanar

489 distances of CGO (1.92 Å) and ESB (1.96 Å), respectively. Δd is 0.04 Å. **c**, variation of out-of-plane lattice parameters

490 as a function of λ . The dash-dotted line is guided to the eyes only.

491

492

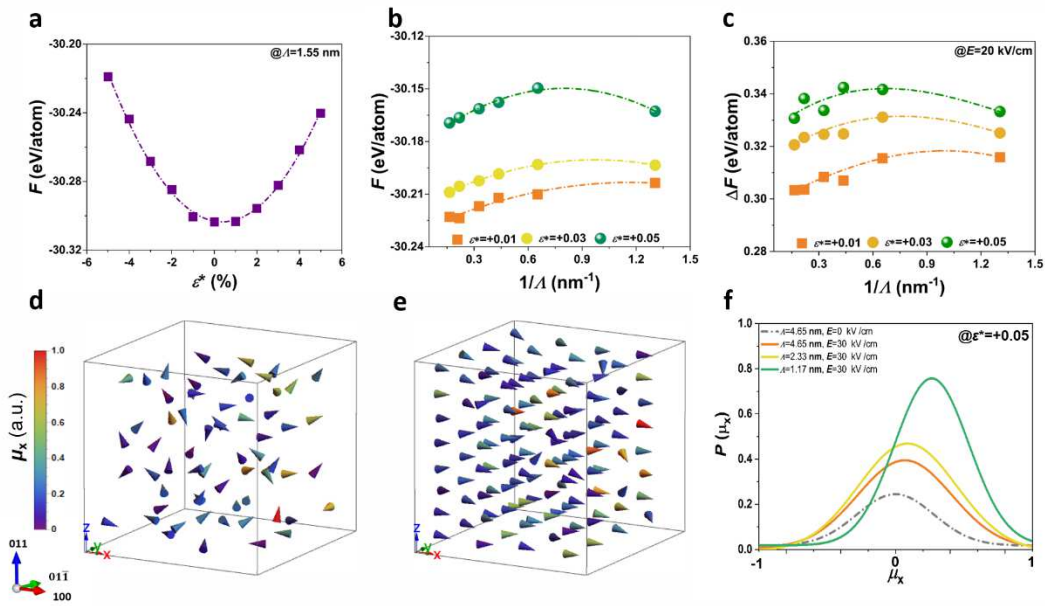
493

494

495

496

497 **Figure 4**



498

499 **Fig. 4 | Mechanism of the enhanced electromechanical response.** a. Free energy (F) for heterostructure with a
 500 modulation length (λ) of 1.55 nm (8 cationic layers). b. Free energy as a function of λ with different biaxial strains
 501 (ϵ^*). c. Free energy change (ΔF) after applying electric field (E) d and e, The distribution of dipoles within the
 502 heterostructure ($1/\lambda = 0.22 \text{ nm}^{-1}$) for $E = 0$ (d) and 30 kV/cm (e) along the $+x$ direction. f. Normalized probability
 503 distribution functions, $P(\mu_x)$ against the normalized dipole moment along the x -axis (μ_x) for heterostructures with
 504 different λ under the same tensile strain ($\epsilon^* = +0.05$). The dash-dotted lines in a, b and c are parabolic fitting to the
 505 calculated results.

Supplementary Files

This is a list of supplementary files associated with this preprint. Click to download.

- [AtomicallyengineeredinterfacesyieldextraordinaryelectrostrictionsupplementaryInformation.pdf](#)
- [AtomicallyengineeredinterfacesyieldextraordinaryelectrostrictionExtendedData.pdf](#)